Tunable Plasmonic Reflection by Bound 1D Electron States in a 2D Dirac Metal

B.-Y. Jiang, G. X. Ni, C. Pan, Z. Fei, B. Cheng, C. N. Lau, M. Bockrath, D. N. Basov, and M. M. Fogler

Phys. Rev. Lett. **117**, 086801 — Published 15 August 2016

DOI: 10.1103/PhysRevLett.117.086801

Tunable plasmonic reflection by bound 1D electron states in a 2D Dirac metal

B.-Y. Jiang,[1] G. X. Ni,[1] C. Pan,[2] Z. Fei,[1,3] B. Cheng,[2] C. N. Lau,[2] M. Bockrath,[2] D. N. Basov,[1,4] and M. M. Fogler[1]

[1]*Department of Physics, University of California San Diego, 9500 Gilman Drive, La Jolla, California 92093*
[2]*Department of Physics, University of California Riverside, 900 University Avenue, Riverside, California 92521*
[3]*Department of Physics, Iowa State University, 2334 Pammel Drive, Ames, Iowa 50011*
[4]*Department of Physics, Columbia University, New York, New York 10027*

(Dated: July 27, 2016)

We show that surface plasmons of a two-dimensional Dirac metal such as graphene can be reflected by line-like perturbations hosting one-dimensional electron states. The reflection originates from a strong enhancement of the local optical conductivity caused by optical transitions involving these bound states. We propose that the bound states can be systematically created, controlled, and liquidated by an ultranarrow electrostatic gate. Using infrared nanoimaging, we obtain experimental evidence for the locally enhanced conductivity of graphene induced by a carbon nanotube gate, which supports this theoretical concept.

Plasmon scattering and plasmon losses in Dirac materials, such as graphene and topological insulators, are problems of interest to both fundamental and applied research. It is an outstanding challenge to understand various kinds of interaction (electron-electron, electron-phonon, electron-photon, electron-disorder) responsible for these complex phenomena [1–5]. At the same time, control of plasmon scattering is critical if this class of materials is to become a new platform for nanophotonics [6–9].

One source of plasmon scattering is long-range inhomogeneity of the electron density, which causes local fluctuations in the plasmon wavelength λ_p. If the inhomogeneities are weak, those of size comparable to the average λ_p are expected to be the dominant scatterers [10, 11] Surprisingly, recent experiments have revealed that one-dimensional (1D) defects of nominally atomic width can act as effective reflectors for plasmons with wavelengths as large as a few hundred nm. Strong plasmon reflection was observed near grain boundaries [12, 13], topological stacking faults [14], as well as nanometer-scale wrinkles and cracks [11, 12] in graphene. If this anomalous reflection is indeed an ubiquitous effect largely unrelated to the specific nature of a defect, it calls for a universal explanation. In this Letter we attribute its origin to electron bound states commonly occurring near 1D defects. We show that optical transitions involving the bound states can produce strong dissipation at small distances x from the defect and therefore, alter plasmon dynamics. To support this idea we present a theoretical analysis of an exactly solvable model, which illustrates qualitative and quantitative characteristics of the bound states and predicts how their optical response depends on the tunable parameters of a 1D potential well. We also report an attempt to probe the predicted effects experimentally. Our approach is to employ an ultranarrow electric gate in the form of a carbon nanotube (CNT) to create a precisely tunable 1D barrier in graphene. This device enables a systematic investigation and control of plasmon propagation, including, in principle, an implementation of a plasmon on-off switch (Fig. 1). What we find is that the measured real-space profile of the plasmon amplitude (Fig. 4) cannot be accounted for by a local change in λ_p alone. Instead, the data are consistent with the presence of an enhanced dissipation in the region next to the CNT. The amount of this dissipation agrees in the order of magnitude with the power absorption due to 1D bound states in our model.

Model.—We assume that the graphene quasiparticles can be described by a 2D Dirac Hamiltonian $H = \hbar v_F(\sigma_z k_x + \sigma_y k_y) + v(x)$, where σ_y, σ_z are the Pauli matrices and $v(x)$ is the total (screened) potential induced by the 1D gate. For simplicity, we assume that $v(x)$ is a square well of width d and depth u although more realistic potentials [15–18] can also be considered. In the present case the eigenfunctions Ψ are combinations of plane waves and/or exponentials that have to be matched at $x = \pm d/2$, see [19]. The electron momentum k_y along the perturbation (in the y-direction) is conserved, so that the gapless 2D Dirac spectrum is effectively replaced by a 1D one with a gap $\Delta = |\hbar v_F k_y|$. Within the gap electron states localized at the well exist [Fig. 2(b)]. The energies $\varepsilon_n(k_y)$ of these bound states, where $n = 1, 2, \ldots$, are the solutions of the transcendental equation [35]

$$\frac{\tan\sqrt{(E+U)^2 - K_y^2}}{\sqrt{(E+U)^2 - K_y^2}} = \frac{i\sqrt{E^2 - K_y^2}}{K_y^2 - E(E+U)}. \tag{1}$$

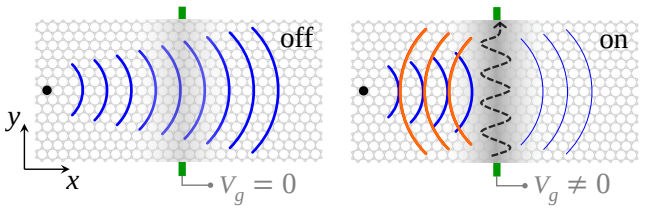

FIG. 1. (Color online) Schematic of an ultranarrow plasmon reflector. The incident plasmon (blue) can propagate freely unless a local perturbation hosting a 1D electron state (the dashed arrow) causes it to be reflected (orange). The bound state parameters are controlled by voltage V_g of a nanotube gate (green).

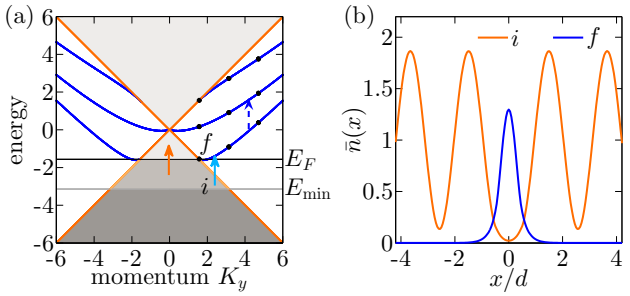

FIG. 2. (Color online) (a) Dispersion of bound states for a sheet (blue) or a ribbon of width $2d$ (the black dots) for $U = 5$. The light gray are empty states in the continuum. The dark and medium gray are occupied states in the continuum. The last of these, with E between $E_F = \mu d/\hbar v_F$ and $E_{\min} = E_F - \omega d/v_F$, enable optical transitions (the arrows) of frequency ω. Transitions between bound states (the dashed arrow) can occur for some E_F, e.g., $E_F = 0$ at which the state i is filled and the state f is empty. (b) The density distribution $\bar{n} = |\Psi|^2$ of the two states i and f for the transition indicated by the cyan arrow in (a). The state i (blue) is localized in the well, while the state f (orange) is extended. Parameters: $K_y = 2.5$, $\omega d/v_F = \pi/2$.

Here $E = \varepsilon_n d/(\hbar v_F)$ is the dimensionless energy and

$$K_y = k_y d\,, \quad U = ud/(\hbar v_F)\,, \tag{2}$$

are, respectively, the dimensionless y-momentum and the well depth. The dispersions of the three lowest bound states for $U = 5$ are shown in Fig. 2(a).

The response of the system to an optical excitation of frequency ω polarized in the x-direction is described by an effective conductivity $\sigma(x)$ given by the Kubo formula [19], which determines the local current density $j_x(x) = E_x\sigma(x)$ in the approximation that the total electric field E_x due to the optical excitation is uniform. Below we focus on the real part of $\sigma(x)$, which determines local power dissipation. We assume that graphene is doped and consider only frequencies $\hbar\omega < 2|\varepsilon_F|$, for which the optical conductivity of an infinite graphene sheet vanishes (if we neglect disorder, many-body scattering, and thermal broadening [3]). This implies that in the absence of the perturbation, $U = 0$, we must have $\mathrm{Re}\,\sigma(x) = 0$ at all x. On the other hand, when the potential well is present, a finite $\mathrm{Re}\,\sigma(x)$ exists. There are two types of relevant optical transitions: those that involve the bound states [as either the initial i or the final f states, Fig. 2(a)] and those that do not. The contribution of the former to $\mathrm{Re}\,\sigma(x)$ is maximized near the potential well and decays exponentially at $|x| > d/2$ due to the localized nature of the bound states. The contribution of the latter is small, oscillating, and decaying algebraically with x [19]. Resolving the detailed real-space features of $\sigma(x)$ in an optical experiment is challenging (see below). A more practical observable is the normalized integrated conductivity:

$$\bar{\sigma} \equiv \frac{1}{d}\int_{-\infty}^{\infty} dx\,\mathrm{Re}\,\sigma(x)\,. \tag{3}$$

According to our simulations, transitions that involve the bound states give the dominant contribution to $\bar{\sigma}$. In particular, bound-to-bound state transitions produce numerically large values of $\bar{\sigma}$ expressed in units of e^2/h. Such transitions are possible at discrete k_y where the energy difference between the states of the same momentum matches $\hbar\omega$ provided the lower (higher) state is occupied (empty). If the chemical potential μ is gradually increased, e.g., by electrostatic gating, the state occupations would change, leading to either blocking or unblocking of these transitions. Accordingly, $\bar{\sigma}$ would either sharply drop or jump, see Fig. 3(a). These changes persist, albeit blurred, at finite temperatures, see the dashed curve in Fig. 3(a).

Sharp drops in $\bar{\sigma}$ also occur when the bound states merge with the continuum and get liquidated (become extended). The drop is abrupt if the optical transitions probe a single k_y or a narrow range of k_y. In principle, this situation can be realized in a graphene ribbon running perpendicular to the linelike perturbation. In such a ribbon the allowed $k_y = m\pi/W + \mathrm{const}$ are discrete, as shown schematically by the dots in Fig. 2(b). The coupling to a single bound state can be achieved under the condition $\pi/W > \omega/v_F$, i.e., by using a ribbon of a narrow width W or the excitation of a low frequency ω. In Fig. 3(b) we show three numerically calculated traces of $\bar{\sigma}$ as a function of the well depth U for a fixed dimensionless chemical potential $E_F = \mu d/(\hbar v_F) = -\pi/2$. The first trace is computed for a ribbon of width $W = 2d$ probed at the excitation energy $\hbar\omega = |\mu|$. It exhibits pronounced oscillations of $\bar{\sigma}$. In particular, $\bar{\sigma}$ drops to zero when a bound state merges with the continuum. The other two traces correspond to a 2D graphene sheet. Although the sharp drops become blurred, they remain pronounced at a low excitation energy $\hbar\omega_1 = |\mu|/10$ and still evident at $\hbar\omega_2 = |\mu|$.

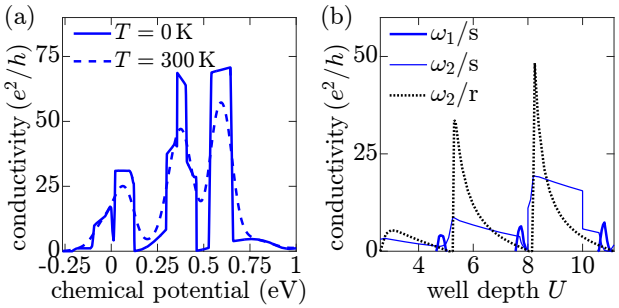

FIG. 3. (Color online) (a) Integrated conductivity $\bar{\sigma}$ of a graphene sheet at $\omega = 830\,\mathrm{cm}^{-1}$. The sharp changes are caused by blocking/unblocking of the transitions involving bound states as a result of changing occupations of the levels as a function of the graphene chemical potential μ. For example, the plateau at $0.02 < \mu(\mathrm{eV}) < 0.12$ is due to the (blue) dashed-line transition in Fig. 2(a). (b) Integrated conductivity $\bar{\sigma}$ of a sheet (s) and a ribbon (r) at $T = 0$ and $K_F = -\pi/2$. Sharp changes at $U = 8$ and 10 for $\omega = \omega_2$ arise from a transition between bound states. Parameters: $d = 10\,\mathrm{nm}$, $\omega_1 = 83\,\mathrm{cm}^{-1}$, $\omega_2 = 830\,\mathrm{cm}^{-1}$.

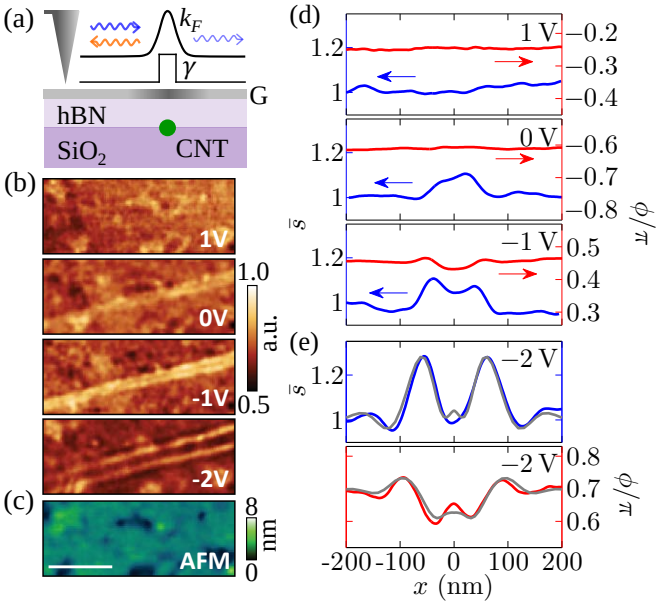

FIG. 4. (Color online) Measurement of the conductivity $\bar{\sigma}$ by the s-SNOM. (a) A schematic showing graphene (variable intensity gray) gated by a CNT (green) separated from it by a thin hBN layer. The induced perturbation is parameterized by spatially varying k_F and γ. In the experiment, the AFM tip (triangle) is polarized by a focused infrared beam (not shown), which enables it to launch a plasmon (blue). The reflected plasmon (orange) causes an additional tip polarization, resulting in a modified optical signal backscattered by the tip and detected in the far field. (b) The s-SNOM amplitude images of the region next to the CNT for $V_g = +1 \ldots -2\,\mathrm{V}$ and $\omega = 890\,\mathrm{cm}^{-1}$. The twin fringes (bright lines) intensify and separate as $|V_g|$ increases. (c) The AFM topography image of the same region. Scale bar: $1\,\mu\mathrm{m}$. (d)-(e) The s-SNOM amplitude ($\bar{s}$) and phase (ϕ) along the line perpendicular to the CNT; $\bar{s}$ is normalized to $x = -200\,\mathrm{nm}$ point. The best theoretical fits (gray) for $V_g = -2\,\mathrm{V}$ are included in (e).

The enhanced local optical conductivity around the 1D gates described above causes plasmons to be strongly reflected. According to the first-order perturbation theory [11, 12, 19], the reflection coefficient r of a normally incident plasmon wave is

$$r_1 \simeq \frac{2\pi i}{\lambda_p} \int_{-\infty}^{\infty} dx \left[\frac{\sigma(x)}{\sigma_\infty} - 1 \right]. \tag{4}$$

For arbitrary perturbations, we can use the approximation $|r| \approx \min(|r_1|, 1)$. Using the results of Fig. 3(b) we estimate $|r| \approx 0.3$ at the chemical potential of 0.25 eV where the predicted $\bar{\sigma} \approx 5e^2/h$. This roughly corresponds to the regime probed by our experiments (see below). At the chemical potential of 0.3 eV where the calculated local conductivity is much larger, $\bar{\sigma} \approx 40e^2/h$, the reflection coefficient should approach unity, realizing the "reflector on" state in Fig. 1.

Experiment and analysis.—To investigate the described above phenomena experimentally we fabricated a nanodevice that contained (bottom to top) a Si/SiO_2 substrate, a 10 nm-thick layer of hexagonal boron nitride (hBN), and a mechanically exfoliated graphene flake. A metallic single-wall CNT was placed between hBN and SiO_2. The local charge density of graphene was tunable by the voltage V_g applied between the CNT and graphene. The average carrier density in graphene $|n| \sim 5 \times 10^{12}\,\mathrm{cm}^{-2}$ was produced by uncontrolled ambient dopants (acceptors) [36]. To infer the local optical conductivity $\sigma(x)$ we used scattering-type scanning near-field optical microscopy (s-SNOM) [3, 37, 38], see Fig. 4(a). The s-SNOM utilizes a tip of an atomic force microscope (AFM) with a radus 25 nm as an optical antenna that couples incident infrared light to graphene plasmons. The backscattered light is analyzed to extract the amplitude $\bar{s}$ and the phase ϕ of the genuine near-field signal, Fig. 4(b,d,e). Crudely speaking, this signal is proportional to the electric field inside the tip-sample nanogap. The variation of this field with the tip position is caused by the standing-wave patterns of surface plasmons [23, 39]. These standing waves are due to the interference of the plasmon waves launched by the tip with the waves reflected by the charge inhomogeneity induced by the CNT. The spacing of the interference fringes is equal to one half of the plasmon wavelength λ_p. The latter is given by $\lambda_p = \mathrm{Re}\,(2\pi/q_p)$, where $q_p(x) = i\kappa\omega/2\pi\sigma(x)$ is the complex plasmon momentum and κ is the average permittivity of the media surrounding graphene [3]. Therefore, s-SNOM images combined with the formula for q_p give a direct estimate of $\mathrm{Im}\,\sigma(x)$. The extraction of $\mathrm{Re}\,\sigma(x)$ requires an electromagnetic simulation of the coupled tip-graphene system, which was done using the numerical algorithm developed previously [12, 19, 23]. To facilitate connection with that previous work, we parametrized the conductivity via

$$\sigma(x) = \frac{e^2 v_F}{\pi\hbar\omega} \frac{i k_F(x)}{1 + i\gamma(x)}, \tag{5}$$

which was modelled after the long-wavelength Drude (intraband) conductivity of graphene [3] with Fermi momentum k_F and dimensionless damping factor γ. The goal of the data analysis was to determine the profiles of $k_F(x)$ and $\gamma(x)$ that yield the best fit to the s-SNOM data. In this parametrization, the presence of the bound states should increase the local damping, so the signature we were looking for was the enhanced value of $\gamma(x)$.

Our experimental data are presented in Fig. 4. The AFM topography image, Fig. 4(c), shows that the CNT does not produce any visible topographic features. However, in the near-field signal, up to two pairs of intereference fringes appear on each side of the CNT [the bright lines in Fig. 4(b)]. Similar twin fringes have been observed in prior s-SNOM imaging [12–14, 36] of linear defects in graphene. Importantly, the intensity and spacing of the fringes we observe here evolve with the CNT voltage V_g, which attests to their electronic (specifically, plasmonic) origin.

In addition to the controlled perturbation induced by the CNT, graphene contains uncontrolled ones due to random defects. To reduce the random noise caused by those, we

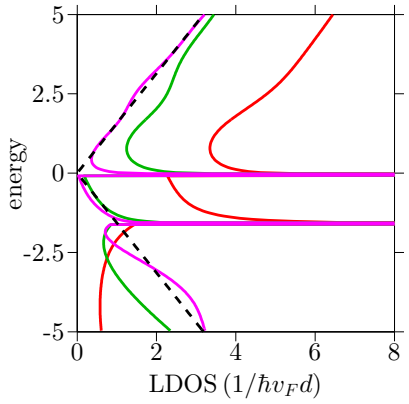

FIG. 5. (Color online) The LDOS as a function of the dimensionless energy E for the $U = 5$ square-well model at the three fixed distances from the CNT: $x/d = 0$ (red), 0.6 (green), and 1.0 (violet). The dashed line shows the LDOS of unperturbed graphene.

averaged the near-field signal over a large number of linear traces taken perpendicular to the CNT. Thus obtained line profiles of both the amplitude $\bar{s}$ and the phase ϕ are plotted in Fig. 4(d) and (e). We focus on the $V_g = -2$V trace, which shows the strongest modulation. The accurate determination of functions $k_F(x)$ and $\gamma(x)$ is impacted by the s-SNOM resolution limit ~ 20nm. In our fitting we assumed that $k_F(x)$ is given by the perfect screening model, $k_F^2(x) = [k_F^2(0)d^2 + k_F^2(\infty)x^2]/(d^2 + x^2)$, which should be a good approximation for high doping [24]. The adjustable parameters are $k_F(0)$ and $k_F(\infty)$. For $\gamma(x)$ we considered trial functions in the form of a peak (dip) at $x = 0$, with adjustable width and height (depth), as sketched in Fig. 4(a). The trial $k_F(x)$ and $\gamma(x)$ were fed as an input to the electromagnetic solver described previously [12, 23]. As detailed in [19], a good agreement with the observed form of the twin fringes requires a strong peak in $\gamma(x)$ near the CNT. The shape of the fringes was found to depend primarily on the integral of $\gamma(x) - \gamma(\infty)$, so in the end we modeled $\gamma(x)$ by a box-like discontinuity with a central region of a fixed width 13.5nm and two adjustable parameters $\gamma(0)$, $\gamma(\infty)$. The best fits [the gray curves in Fig. 4(e)] to the $V_g = -2$V s-SNOM data were obtained using $\gamma(0) = 1.65$.

To establish a rough correspondence between the profiles of Fig. 4(e) and the square-well model we take d to be the thickness of the hBN spacer $d = 10$nm and U to give the same integrated weight $\int v(x)dx \equiv ud = \hbar v_F U = \hbar v_F \int [k_F(x) - k_F(\infty)]dx$. This prescription implies $E_F = 4$, $U = 13$, and $\bar{\sigma} = 3.5\,e^2/h$ for $\omega = 890\,\mathrm{cm}^{-1} = 1.7 v_F/d$ [19]. The square-well model in Fig. 3 yields a comparable optical conductivity $\bar{\sigma} = 4.7\,e^2/h$ although for a smaller $U = 5$. Given a number of simplifying assumptions we have made in the modelling, this level of agreement seems adequate.

Summary and future directions.—In this Letter, we proposed a model for the anomalous plasmon reflection by ultranarrow electron boundaries in graphene. We validated this concept in experiments with electrostatically tunable line-like perturbations. One broad implication of our work is that nanoimaging of collective modes can reveal nontrivial electron properties, in this case, 1D bound states. Recent experiments have demonstrated that this technique is not limited to plasmons or graphene or 2D systems [40–43]. We hope that our work stimulates even wider use of this novel spectroscopic tool.

A particularly intriguing future direction is to complement s-SNOM with scanned probe techniques other than AFM topography. For example, scanning tunneling microscopy, which has a superior spatial resolution, can be used to measure the local electron density of states (LDOS). For the particular model system studied here, the features exhibited by the LDOS should be quite striking, see Fig. 5 and [19]. The origin of these features can be understood by examining the dispersions in Fig. 2(a). Within the selected energy interval there is the total of three bound states. The topmost one has a monotonic dispersion; the other two have energy minima at which the LDOS has van Hove singularities (diverges), see Fig. 5. The strength of these singularities decreases exponentially with x because these bound states are localized near the well. At large x, the LDOS displays the V-shaped energy dependence characteristic of uniform graphene [3]. We anticipate that the combination of optical and tunneling nanoimaging and nanospectroscopy could provide a refined information about the local electronic structure. One example of a possible application of this knowledge is the design of optimized plasmon switches (Fig. 1) for Dirac-material-based nanoplasmonics.

We acknowledge support by the ONR under Grant N00014-13-0464 and by the NSF under Grant ECCS-1509958 (M.B.).

[1] S. Das Sarma, S. Adam, E. H. Hwang, and E. Rossi, Rev. Mod. Phys. **83**, 407 (2011).
[2] V. N. Kotov, B. Uchoa, V. M. Pereira, F. Guinea, and A. H. Castro Neto, Rev. Mod. Phys. **84**, 1067 (2012).
[3] D. N. Basov, M. M. Fogler, A. Lanzara, F. Wang, and Y. Zhang, Rev. Mod. Phys. **86**, 959 (2014).
[4] A. Principi, M. Carrega, M. B. Lundeberg, A. Woessner, F. H. L. Koppens, G. Vignale, and M. Polini, Phys. Rev. B **90**, 165408 (2014).
[5] A. Woessner, M. B. Lundeberg, Y. Gao, A. Principi, P. Alonso-González, M. Carrega, K. Watanabe, T. Taniguchi, G. Vignale, M. Polini, J. Hone, R. Hillenbrand, and F. H. L. Koppens, Nature Mater. **14**, 421 (2014).
[6] M. Jablan, H. Buljan, and M. Soljačić, Phys. Rev. B **80**, 245435 (2009).
[7] A. Vakil and N. Engheta, Science **332**, 1291 (2011).
[8] A. N. Grigorenko, M. Polini, and K. S. Novoselov, Nature Photon. **6**, 749 (2012).
[9] F. J. García de Abajo, ACS Photon. **1**, 135 (2014).
[10] K. Kechedzhi and S. Das Sarma, Phys. Rev. B **88**, 085403 (2013).
[11] J. L. Garcia-Pomar, A. Y. Nikitin, and L. Martin-Moreno, ACS Nano **7**, 4988 (2013).

[12] Z. Fei, A. S. Rodin, W. Gannett, S. Dai, W. Regan, M. Wagner, M. K. Liu, A. S. McLeod, G. Dominguez, M. Thiemens, A. H. Castro Neto, F. Keilmann, A. Zettl, R. Hillenbrand, M. M. Fogler, and D. N. Basov, Nature Nano. **8**, 821 (2013).

[13] M. Schnell, P. S. Carney, and R. Hillenbrand, Nature Comm. **5**, 3499 (2014).

[14] L. Ju, Z. Shi, N. Nair, Y. Lv, C. Jin, J. Velasco, C. Ojeda-Aristizabal, H. A. Bechtel, M. C. Martin, A. Zettl, J. Analytis, and F. Wang, Nature **520**, 650 (2015).

[15] P. Kennedy, J. Phys. A **35**, 689 (2002).

[16] R. R. Hartmann and M. E. Portnoi, Phys. Rev. A **89**, 012101 (2014).

[17] N. Candemir and O. Bayrak, J. Math. Phys. **54**, 042104 (2013).

[18] V. M. Villalba and W. Greiner, Phys. Rev. A **67**, 052707 (2003).

[19] See Supplemental Material at [URL will be inserted by publisher] which includes the calculation of $\bar{\sigma}$, ν, the s-SNOM data analysis, and Refs. [20-34].

[20] B. Wunsch, T. Stauber, F. Sols, and F. Guinea, New J. Phys. **8**, 318 (2006).

[21] Y. Wang, D. Wong, A. V. Shytov, V. W. Brar, S. Choi, Q. Wu, H.-Z. Tsai, W. Regan, A. Zettl, R. K. Kawakami, S. G. Louie, L. S. Levitov, and M. F. Crommie, Science **340**, 734 (2013).

[22] A. V. Shytov, M. I. Katsnelson, and L. S. Levitov, Phys. Rev. Lett. **99**, 246802 (2007).

[23] Z. Fei, A. S. Rodin, G. Andreev, W. Bao, A. S. McLeod, M. Wagner, L. Zhang, Z. Zhao, M. Thiemens, G. Dominguez, M. M. Fogler, A. H. Castro Neto, C. Lau, F. Keilmann, and D. N. Basov, Nature **487**, 82 (2012).

[24] B.-Y. Jiang and M. M. Fogler, Phys. Rev. B **91**, 235422 (2015).

[25] J.-W. Huang, C. Pan, S. Tran, B. Cheng, K. Watanabe, T. Taniguchi, C. N. Lau, and M. Bockrath, Nano Lett. **15**, 6836 (2015).

[26] Y. B. Zeldovich and V. S. Popov, Sov. Phys. Uspekhi **14**, 673 (1972).

[27] A. V. Shytov, M. I. Katsnelson, and L. S. Levitov, Phys. Rev. Lett. **99**, 236801 (2007).

[28] V. M. Pereira, J. Nilsson, and A. H. Castro Neto, Phys. Rev. Lett. **99**, 166802 (2007).

[29] M. M. Fogler, D. S. Novikov, and B. I. Shklovskii, Phys. Rev. B **76**, 233402 (2007).

[30] A. De Martino, D. Klöpfer, D. Matrasulov, and R. Egger, Phys. Rev. Lett. **112**, 186603 (2014).

[31] E. V. Gorbar, V. P. Gusynin, and O. O. Sobol, Phys. Rev. B **92**, 235417 (2015).

[32] J. R. S. Nascimento, I. Cho, and A. Vilenkin, Phys. Rev. D **60**, 083505 (1999).

[33] V. M. Pereira, A. H. Castro Neto, H. Y. Liang, and L. Mahadevan, Phys. Rev. Lett. **105**, 156603 (2010).

[34] B. Chakraborty, K. S. Gupta, and S. Sen, J. Phys. Conf. Ser. **442**, 012017 (2013).

[35] C. W. J. Beenakker, R. A. Sepkhanov, A. R. Akhmerov, and J. Tworzydło, Phys. Rev. Lett. **102**, 146804 (2009).

[36] G. X. Ni, H. Wang, J. S. Wu, Z. Fei, M. D. Goldflam, F. Keilmann, B. Özyilmaz, A. H. Castro Neto, X. M. Xie, M. M. Fogler, and D. N. Basov, Nature Mater. **14**, 1217 (2015).

[37] F. Keilmann and R. Hillenbrand, "Nano-optics and Near-field Optical Microscopy," (Artech House, Norwood, 2009) Chap. 11: Near-Field Nanoscopy by Elastic Light Scattering from a Tip, pp. 235–266, edited by A. Zayats and D. Richards.

[38] J. M. Atkin, S. Berweger, A. C. Jones, and M. B. Raschke, Adv. Phys. **61**, 745 (2012).

[39] J. Chen, M. Badioli, P. Alonso-Gonzalez, S. Thongrattanasiri, F. Huth, J. Osmond, M. Spasenovic, A. Centeno, A. Pesquera, P. Godignon, A. Zurutuza Elorza, N. Camara, F. J. García de Abajo, R. Hillenbrand, and F. H. L. Koppens, Nature **487**, 77 (2012).

[40] S. Dai, Z. Fei, Q. Ma, A. S. Rodin, M. Wagner, A. S. McLeod, M. K. Liu, W. Gannett, W. Regan, M. Thiemens, G. Dominguez, A. H. Castro Neto, A. Zettl, F. Keilmann, P. Jarillo-Herrero, M. M. Fogler, and D. N. Basov, Science **343**, 1125 (2014).

[41] Z. Shi, X. Hong, H. A. Bechtel, B. Zeng, M. C. Martin, K. Watanabe, T. Taniguchi, Y.-R. Shen, and F. Wang, Nature Photon. **9**, 515 (2015).

[42] A. J. Giles, S. Dai, O. J. Glembocki, A. V. Kretinin, Z. Sun, C. T. Ellis, J. G. Tischler, T. Taniguchi, K. Watanabe, M. M. Fogler, K. S. Novoselov, D. N. Basov, and J. D. Caldwell, Nano Lett. **XX**, XXX (2016).

[43] Z. Fei, M. Scott, D. J. Gosztola, J. J. Foley, J. Yan, D. G. Mandrus, H. Wen, P. Zhou, D. W. Zhang, Y. Sun, J. R. Guest, S. K. Gray, W. Bao, G. P. Wiederrecht, and X. Xu, "Nano-optical imaging of exciton polaritons inside WSe_2 waveguides," arXiv:1601.02133.